OPEN

$Mn_3[Co(CN)_6]_2@SiO_2$ Core-shell Nanocubes: Novel bimodal contrast agents for MRI and optical imaging

Yimin Huang[1], Lin Hu[2], Tingting Zhang[3], Hao Zhong[1], Jiajia Zhou[4], Zhenbang Liu[4], Haibao Wang[3], Zhen Guo[4] & Qianwang Chen[1,2]

[1]Hefei National Laboratory for Physical Sciences at Microscale and Department of Materials Science & Engineering, University of Science and Technology of China, Hefei 230026, China, [2]High Magnetic Field Laboratory, Hefei Institutes of Physical Science, Chinese Academy of Sciences, Hefei 230031, China, [3]Radiology Department of the First Affiliated Hospital of Anhui Medical University, Hefei 230022, China, [4]Anhui Key Laboratory for Cellular Dynamics and Chemical Biology, School of Life Sciences, University of Science and Technology of China, Hefei 230027, China.

Nanoprobes with dual modal imaging of magnetic resonance imaging (MRI) and two-photon fluorescence (TPF) can serve as promising platforms for clinical diagnosis. A wide range of molecules and nanoparticles have been investigated as agents for contrast enhanced MRI and fluorescence imaging in cancer diagnosis. However, a single material with dual modal imaging of MRI and TPF is rarely reported. We found that $Mn_3[Co(CN)_6]_2$ nanocubes can serve as agents for both T_1- and T_2-weighted MRI, and TPF imaging. The nanocubes coated with silica to form $Mn_3[Co(CN)_6]_2@SiO_2$ core-shell nanocubes were readily internalized by cells without showing cytotoxicity. In vitro tests, the core-shell nanocubes display relatively high longitudinal (r_1) and transverse (r_2) relaxivities, they also manifest a remarkable T_1 and T_2 contrast effects at in-vivo imaging of internal organs in Mice. Moreover, the core-shell nanocubes could offer high-resolution cell fluorescence imaging by two-photon excitation (720 nm) or by conventional fluorescence with 403- or 488-nm excitation.

Medical imaging in early detection has become crucial in the fight against cancer. Among various molecular imaging techniques, magnetic resonance imaging (MRI) and fluorescence optical imaging (FOI) are the most commonly used imaging approaches[1–4], which can distinguish fine variations in tissues within the body and provide detailed information on the dynamics of cellular interactions[5–7]. However, sometimes, the difference between normal and abnormal tissue is too small to be distinguished, which raises the demand of contrast agents (CAs) to differentiate between target and background for in-vivo bio-imaging[8]. CAs can depict anatomic details conserving high spatial resolution without the loss of signal and finally maximizing the ability of MRI due to the signal-enhancing positive contrast ability[9]. Two types of MRI contrast agents, paramagnetic coordination complexes and superparamagnetic nanoparticles, are currently used in practice[10]. For example, paramagnetic gadolinium (Gd^{3+}) complexes (e.g. gadolinium diethylene-triaminepentaacetate (Gd-DTPA) ($r_1 = 4$ mM^{-1} sec^{-1}) are most widely used as T_1 MRI CAs in clinical practice, which can provide outstanding positive MR images with high resolution[11–13]. Unfortunately, some discoveries have shown Gd^{3+} could be involved in nephrogenic systemic fibrosis (NSF), which would limit their megadose clinical applications[14]. Other biocompatible materials such as manganese oxide nanoparticles (e.g. water-dispersible MnO with $r_1 = 0.21$ mM^{-1} sec^{-1} and MnO hollow particles with $r_1 = 0.353$ mM^{-1} sec^{-1}) could also be used as T_1 contrast agents. However, extremely low longitudinal relaxivity (r_1) of manganese oxide nanoparticles has severely hindered their applications as CAs for the cytotoxicity associated with a high-dose nanoparticles required[15,16]. Typical T_2 CAs are superparamagnetic iron oxide nanoparticles (SPIO), which can provide very sensitive T_2-weighted images to detect lesions from normal tissues[17,18]. However, T_2 agents provide dark negative signal intensity in images, which is often confused with the signals from bleeding and calcification[19]. To overcome these disadvantages, major efforts have been made in recent years to integrate T_1 and T_2 CAs together to form dual modal contrast agents (DMCAs), T_1-weighted imaging is very sensitive at finding a diseased tissue, while T_2-weighted imaging can define tumors in clinic applications[20]. Currently, DMCAs are prepared through the integration of iron oxide nanoparticles and Gd species in a "core-shell" format[21]. Recently, Fe_3O_4/MnO hybrid nanocrystals have also been prepared as DMCAs[22]. Unfortunately, it was reported that the "core-shell" structure is apt to cause undesirable interactions between the superparamagnetic and paramagnetic nanoparticles, which can decrease the relaxivity of

T_1 signal[23]. Although it has been reported that monodisperse Gd_2O_3-embedded iron oxide (GdIO) nanoparticles as DMCAs with high r_1 values is a solution to this problem, the mixture of precursors cannot ensure Gd_2O_3 uniformly distributed in iron oxide nanoparticles. Furthermore, the synthetic process of core-shell DMCAs is complicated, and the surfactants used to assist synthesis is difficult to be removed, which may increase potential hazards to human health.

Two-photon laser scanning microscopy (TPLSM) has also become an indispensable tool for direct observation of cellular structure and biological process with the advantages of larger penetration depth in biological tissues, more reduction of photobleaching and weak autofluorescence[24]. The cellular imaging application of TPLSM has been investigated using inorganic quantum dots (QDs), metallic nanoparticles and organic dyes or pigments as probes[25–27]. Even though various targeting ligands have been labeled with these probes to delineate tumor margins to improve surgical outcome, preoperative diagnostic images cannot be correlated with intraoperative pathology[28].

In a word, each imaging modality has advantages and limitations regarding sensitivity, resolution, and tissue penetration of signal. Dual modal imaging combining MRI/fluorescent probes can overcome the limitations of each modality[29]. Researchers usually prefer to conjunct fluorescent organic dyes with already prepared MRI CAs to develop such dual probes. For example, such probes have been synthesized by combining mesoporous silica-coated hollow manganese oxide nanoparticles with rhodamine B isothiocyanate (RITC) or $Ru(bpy)_3^{2+}$ (fluorescent probes)[30,31], doping SPIO nanocrystals with fluorescein isothiocyanate (FITC)[32] and coating Fe_3O_4 cores or MnO nanoflowers with Au shells[33,34]. It is reported that the combination of SPIO nanoparticles with QDs or noble metal nanoparticles (e.g. Ag) can also produce dual functional CAs[35,36]. However, there are several drawbacks of such composite nanoparticles, which include: 1) The combining process is complicated; 2) The surfactants used during the preparation, e.g. CTAB and EDAC, are known to be cytotoxic[37,38]; 3) The attached fluorescent probes can drop off, with the potential of causing damage to human health; 4) The organic dye is not stable enough, for example, FITC is easily quenched in an acidic buffer; 5) Even though various post-synthesis modifications have been done, the cytotoxicity of some composite nanoparticles is still high.

The best way to overcome the problems highlighted above is to combine all those MRI and FOI properties in single-material nanoparticles instead of composite nanoparticles. The overall goal of this study is to develop a single-material nanoparticles-based platform for multimodal imaging. It has been reported that Prussian blue nanoparticles exhibit a T_1 contrast effect, the unique structure of metal organic frameworks (MOFs) may bring strong interactions between ion centers and water protons, inducing MRI contrast enhancement[39]. Taking into consideration the MRI properties of hollow MnO nanoparticles[40], it is reasonable to suggest that MOF compounds containing Mn^{2+} ions have the potential to be used as DMCAs. Moreover, Mn^{2+} doped QDs represent a class of phosphors that have already been utilized for many applications[41,42]. Thus, nanocubes of $Mn_3[Co(CN)_6]$ were prepared and their applications as multimodal imaging contrast agents were explored. To further enhance their biocompatibility, silica coating process has been applied to form core-shell nanocubes, $Mn_3[Co(CN)_6]_2@SiO_2$.

Results

$Mn_3[Co(CN)_6]_2$ nanocubes were synthesized at room temperature[43] and coated by treating the nanocubes with TEOS under sol-gel conditions (Supporting Information, Scheme 1). Field-effect scanning electron microscope (FE-SEM) images showed that uniform $Mn_3[Co(CN)_6]_2$ and $Mn_3[Co(CN)_6]_2@SiO_2$ nanocubes with the size around 150–180 nm and 160–200 nm were obtained, respectively (Figure 1). Some cracks (shown by the red arrow in Figure 1b) on the surface appeared along with the increase of pore size after silica coating to form $Mn_3[Co(CN)_6]_2@SiO_2$ nanocubes (Supplementary

Table 1). The molar ratio of Mn to Co was measured to be approximately 3 : 2 (Supplementary Table 2) by inductively coupled plasma-atomic emission spectrometry (ICP-AES) and was consistent with the X-ray powder diffraction (XRD) phase analysis (Supplementary Fig. 1). The silica coating cannot be detected by XRD due to its amorphous nature with a very weak and broad diffraction band at $20°$, however, the peak at 102.90 eV in X-ray photoelectron spectroscopy (XPS) spectra corresponds to chemical bonding of Si-O, which confirmed the existence of silica (Supplementary Fig. 2). Transmission electron microscopy (TEM) images were applied to substantiate the core-shell format of $Mn_3[Co(CN)_6]_2@SiO_2$ nanocube (Supplementary Fig. 3a, b and inset). Energy Dispersive Spectrometer (EDS) pattern comfirmed the surface element distribution of manganese (Mn), cobalt (Co), silicium (Si) and oxygen (O) in $Mn_3[Co(CN)_6]_2@SiO_2$ nanocube, showing the existence of the silica layer (Supplementary Fig. 3c). Both uncoated and silica-coated $Mn_3[Co(CN)_6]_2$ nanocubes displayed relatively high surface area and large pore size, measured by nitrogen absorption–desorption isotherms at 77 K (Supplementary Fig. 4). The nanocubes can form stable colloidal suspensions in aqueous media, which can be used days later (Supplementary Fig. 5).

Biocompatibility without cytotoxicity is an important property of materials for biomedical applications. To evaluate the cytotoxicity of the as-prepared nanocubes, 3-(4,5-Dimethylthiazol-2-yl)-2,5-diphenyltetrazolium bromide (MTT) assays were carried on HeLa, Hep-G2, A549 and glioma C6 cell lines. As shown in Figure 2, these cell lines remain highly viable after being incubated for 24 h, indicating that for the tested concentrations there is no cytotoxicity. Although Mn, Co and CN^- may be toxic, their toxicity can be significantly reduced when forming coordination compounds such as $Mn_3[Co(CN)_6]_2$ nanocubes that are composed by stable chemical bonds. What's more, the biotoxicity of silica-coated $Mn_3[Co(CN)_6]_2$ nanocubes can be further reduced, especially at higher concentrations.

Uncoated and silica-coated $Mn_3[Co(CN)_6]_2$ nanocubes as DMCAs for MRI have been investigated both in-vitro and in-vivo. The MRI signal intensity of samples was measured by a 3T MRI scanner. Uncoated and silica-coated $Mn_3[Co(CN)_6]_2$ nanocubes were respectively dispersed in pH 7.4 phosphate buffered solutions (PBS) with different concentration of Mn^{2+} to determine the longitudinal (r_1) and transverse (r_2) relaxivities. To quantitatively characterize their magnetic resonance properties, the concentration of Mn^{2+} was measured by ICP-AES. The in-vitro MR images (Figure 3a, b, c, d) demonstrated the relationship between the concentration of Mn^{2+} ions and MR imaging performance. On a per mM Mn^{2+} basis, uncoated and silica-coated $Mn_3[Co(CN)_6]_2$ nanocubes exhibited r_1 of 4.798 $mM^{-1}s^{-1}$ and 10.52 $mM^{-1}s^{-1}$ and r_2^* of 89.5572 $mM^{-1}s^{-1}$ and 173.09 $mM^{-1}s^{-1}$, respectively. It is particularly notable that the minimum dosage that can manifest the contrast over water proton is only 2.5 μg/mL for both types of nanocubes, which shows negligible toxicity at this concentration in cytotoxicity test. HeLa cells were also incubated with various concentrations of $Mn_3[Co(CN)_6]_2@SiO_2$ nanocubes for 24 hours (Supplementary Fig. 6) for further MRI tests. The results obtained are in accordance with results from the in vitro MRI tests. It is demonstrated for the first time that $Mn_3[Co(CN)_6]_2$ nanocubes have the potential to be used as effective T1 & T2 MRI contrast agents.

Effects of $Mn_3[Co(CN)_6]_2@SiO_2$ nanocubes on in-vivo MR imaging were studied in mice with C6 glioma bearing brain tumor with a suspension of 0.5 mL $Mn_3[Co(CN)_6]_2@SiO_2$ nanocubes injected (1.25 mg nanocubes per kilogram of mouse body weight). As the blood brain barrier is destroyed as a result of the tumor formation in this animal model, $Mn_3[Co(CN)_6]_2@SiO_2$ nanocubes enter the tumor readily and are retained there for long periods. Thus, the brain cancer cells were selectively enhanced in T_1 MRI because $Mn_3[Co(CN)_6]_2@SiO_2$ nanocubes were injected through tail vein and accumulated at the tumor by strong cytophagy effect of the
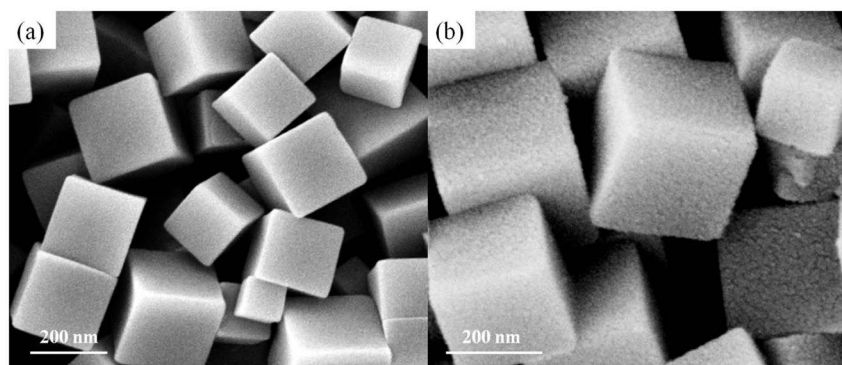
Figure 1 | (a) SEM image of $Mn_3[Co(CN)_6]_2$ nanocubes; (b) SEM image of $Mn_3[Co(CN)_6]_2@SiO_2$ nanocubes.

cancer cells. The localization of nanoparticles in brain tumor tissue was confirmed by ex-vivo ICP measurements, with the concentrations of Mn and Co at approximately 0.19 μg/ml and 0.13 μg/ml, respectively. Based on the images taken from coronal plane (**Figure 4**), within 30 minutes after injection, obvious T_1 contrast effects can be observed at the tumor and remain for 24 hours as the nanocubes accumulating. However, influenced by the bleeding and edema in brain tissue, T_2 effect was not clearly detected. Therefore, in order to evaluate T_2 contrast in tumor imaging of the nanocubes, a perfusion weighted imaging (PWI) was used (**Supplementary Fig. 7**). The T_2 signal was measured every second after the injection of $Mn_3[Co(CN)_6]_2@SiO_2$ nanocubes through tail vein. The signal decreased sharply 11 s post injection, reached the lowest value at 16 s, then

returned back immediately, confirming the T_2 relaxation effects of as-prepared nanocubes. When we compared the signal intensity of brain tumors with normal brain tissue, it was observed that the signal amplitude of T_2 decreased over time because of the abundant vessel and large blood volume at the tumor. It needs to be emphasized that the nanoparticles appeared unlikely to cause acute or severe toxic effects to cause sudden death in mice during in-vivo experiments. No obvious dose-dependent body weight loss in mice was observed. $Mn_3[Co(CN)_6]_2@SiO_2$ nanocubes demonstrated low acute toxicities, thus, can be used as contrast agents.

In order to further demonstrate $Mn_3[Co(CN)_6]_2@SiO_2$ nanocubes with a high r1 relaxivity, we also investigated in-vivo vessel wall imaging of a mouse. $Mn_3[Co(CN)_6]_2@SiO_2$ nanocubes (1.25 mg
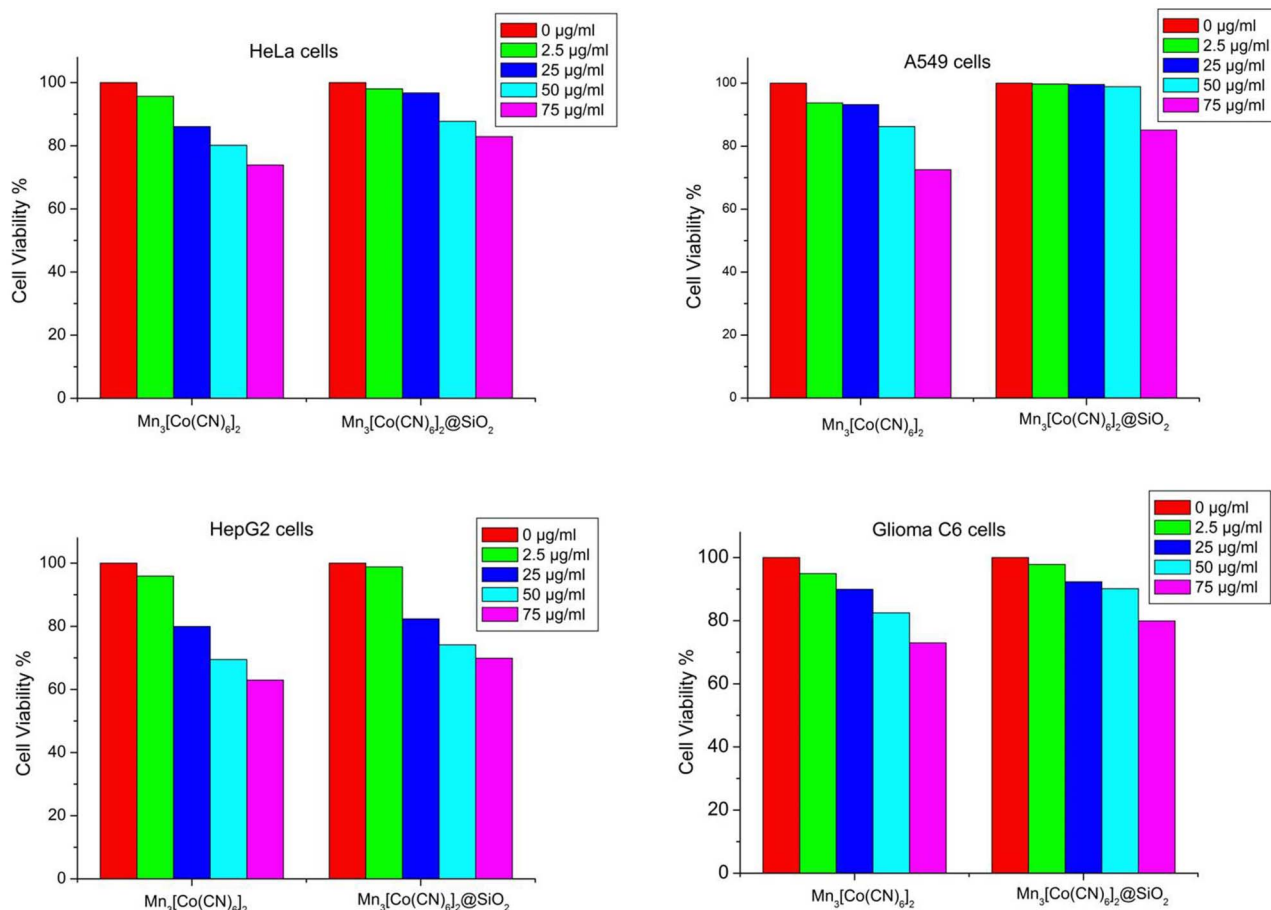

Figure 2 | **Cytotoxicity test of as-prepared $Mn_3[Co(CN)_6]_2$ and $Mn_3[Co(CN)_6]_2@SiO_2$ nanocubes on the viability of HeLa, HepG2, A549 and glioma C6 cells, as measured by MTT assay.**

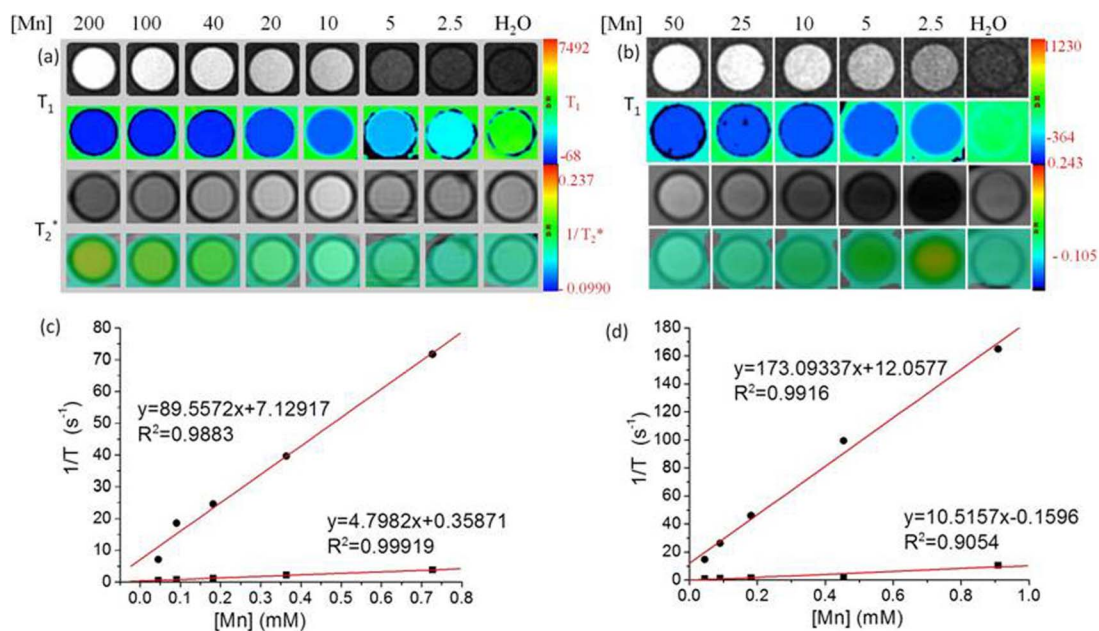Figure 3 | **In vitro MRI test.** (a), (b) T_1 and T_2^* weighted MR images of $Mn_3[Co(CN)_6]_2$ and $Mn_3[Co(CN)_6]_2@SiO_2$ nanocubes with different concentrations of Mn, respectively; c), d) T_1 and T_2^* relaxation rates as a function of Mn concentration of $Mn_3[Co(CN)_6]_2$ and $Mn_3[Co(CN)_6]_2@SiO_2$ nanocubes, respectively.

nanocubes per kilogram of mouse body weight) were injected into a mouse via the tail vein and measured by MR angiography immediately. Blood vessels were clearly seen on T_1-weighted images, displaying outstanding T_1 relaxation properties of $Mn_3[Co(CN)_6]_2@SiO_2$ nanocubes as intravascular MRI CAs (**Figure 5b**). Dynamic changes in signal intensity in the kidney were also clearly observed on T_1-weighted imaging after the injection (**Figure 5a**). By comparing each pair of MRI images before and after $Mn_3[Co(CN)_6]_2@SiO_2$ nanocubes injection, a signal increase is observed on T_1-weighted MR images of a mouse kidney 5 minutes post injection, then the image signals remain stable for 30 minutes. These results

demonstrate for the first time that $Mn_3[Co(CN)_6]_2@SiO_2$ nanocubes have potential for use as T_1 & T_2 MRI contrast agents.

The nanocubes were incubated with HeLa cell lines for 24 h without any further dyeing for TPLSM test by confocal laser scanning microscopy (CLSM). It was observed that uncoated and silica-coated $Mn_3[Co(CN)_6]_2$ nanocubes were localized in cytoplasm and the fluorescence from unstained cells excited at various wavelengths were caused by the nanocubes themselves (**Figure 6**). The emission spectrum in the wavelength range 400 to 720 nm ($\lambda_{ex} = 720$ nm, two photons excitation) was measured by two-photon excited fluorescence microscopy (TEFM) (**Supplementary Fig. 8**). Fluorescence
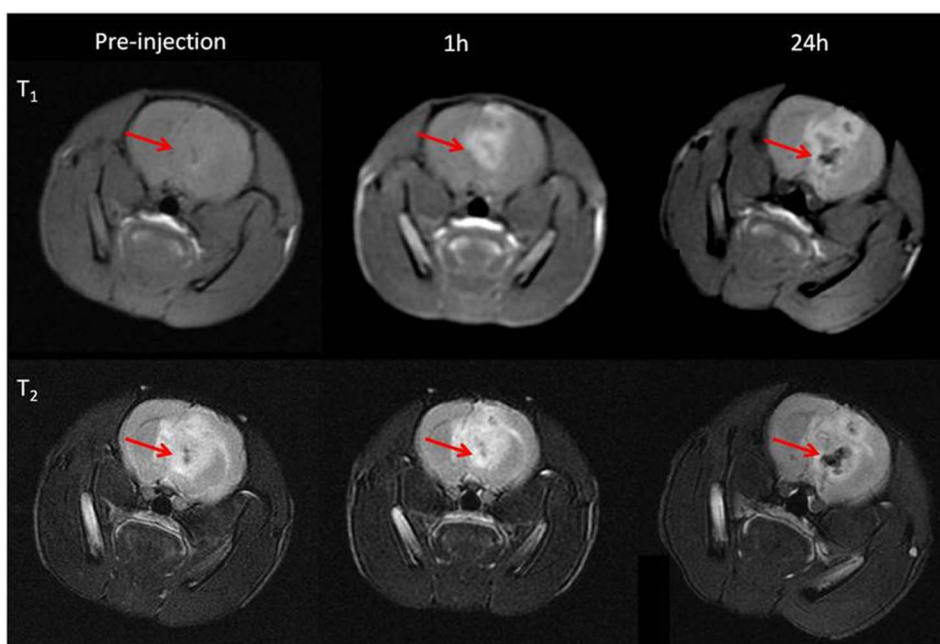

Figure 4 | **MRI signal time courses of T_1 (upper) and T_2 (lower) of a mouse brain bearing the glioma C6 brain tumor that was intravenously injected a suspension of 0.5 mL $Mn_3[Co(CN)_6]_2@SiO_2$ nanocubes in preinjection, 1 h and 24 h after injection.**
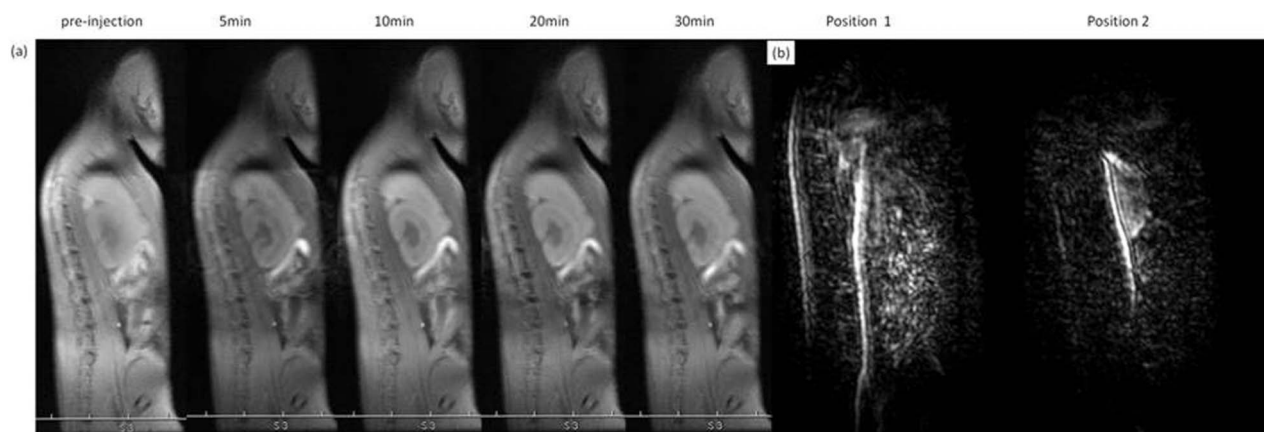
Figure 5 | In vivo MRI images of a mouse injected with Mn$_3$[Co(CN)$_6$]$_2$@SiO$_2$ nanocubes. (a) The time course of the signal enhancement in T$_1$ MRI of a mouse kidney after intravascular injection of Mn$_3$[Co(CN)$_6$]$_2$@SiO$_2$ nanocubes; (b) Intravascular MR angiography images in postcava of the mouse after injecting Mn$_3$[Co(CN)$_6$]$_2$@SiO$_2$ nanocubes through tail vein.

spectra of uncoated and silica-coated Mn$_3$[Co(CN)$_6$]$_2$ nanocubes in the concentration of 250 μg/mL also confirmed that the fluorescence was caused by Mn^{2+} ion, whose emission peaks were around 550–600 nm. The excitation spectra were determined by varying the excitation wavelength to find the maximum emission intensity at 571 nm (**Supplementary Fig. 9a,b**). Two peaks at 355 nm and 475 nm detected in the excitation spectrum were assigned with $^6A_1(^6S) \rightarrow {}^4E(^4D)$ (350 nm, 3.49 eV) and $^6A_1(^6S) \rightarrow {}^4E, {}^4A_1(^4G)$ (475 nm, 2.61 eV) transition of Mn^{2+}, respectively (**Supplementary Fig. 9c,d**). Thus, the luminecence mechanism of as-prepared CAs can be well explained.

Discussion

MRI is currently one of the most powerful imaging technologies both in biological investigations and medical diagnosis. As a new MRI CA, the r$_1$ value of Mn$_3$[Co(CN)$_6$]$_2$@SiO$_2$ nanocubes is much higher than Mn-based CAs. Even though the relaxivity is not as high as that of Gd^{3+} with various ligands (higher than 10 mM^{-1}s^{-1})[44], it is higher than the average value of MnO (lower than 1 mM^{-1}s^{-1})[45,46]. It is interesting to understand why the high r$_1$ value and r$_2$/r$_1$ relaxivity ratio can be generated in the nanocubes. As we know, the interaction dynamics between water and Mn^{2+} complexes highly affects the relaxivity, while the mechanism remains unclear. Based on Solomon-Bloembergen-Morgan (SBM) theory[47,48], direct water coordination to the paramagnetic metal centers is the major contributor to T$_1$ inner-sphere relaxivity[49]. Mn$_3$[Co(CN)$_6$]$_2$ nanocubes have a face-centered cubic structure in which two different ion centers Mn^{2+} and Co^{3+} are bridged by CN$^-$ groups to form an extended 3D covalent coordination lattice structure[39]. As a result, there are a large amount of original pores and voids inside the structure confirmed by pore size distribution measurements. The vacant sites in the lattice are usually occupied by water molecules, which are accessible for water motion, therefore, a well-working inner sphere T$_1$ relaxation of the nanocubes and water molecules can be generated. What's more, the Mn^{2+} ions are positioned in the body centers and edge centers in the face-centered cubic structure, which is free to adjunct with water molecules to form a coordination sphere with each Mn^{2+} ion surrounded with water molecules, thus, the outer sphere T$_1$ relaxation has also been generated. With the simultaneous action of inner and outer sphere relaxation, Mn$_3$[Co(CN)$_6$]$_2$ nanocubes manifest an enhanced relaxivity. Moreover, it is suggested that the higher relaxivity of Mn$_3$[Co(CN)$_6$]$_2$@SiO$_2$ nanocubes is benefited from the silica coating, which allows better water molecules exchange with the metal ions. It has been reported that water molecules diffusing anisotropically inside the silica, with the fastest diffusion component occurring along the channels in the silica, is more rapid than that of the isotropic diffusion in the surrounding environment[30]. Nanopores in Mn$_3$[Co(CN)$_6$]$_2$@SiO$_2$ nanocubes reveraled by nitrogen absorption isotherms measurement allow water molecules diffusion to the magnetic cores, leading to efficient relaxation of water molecules in the vicinity of the nanoparticles.
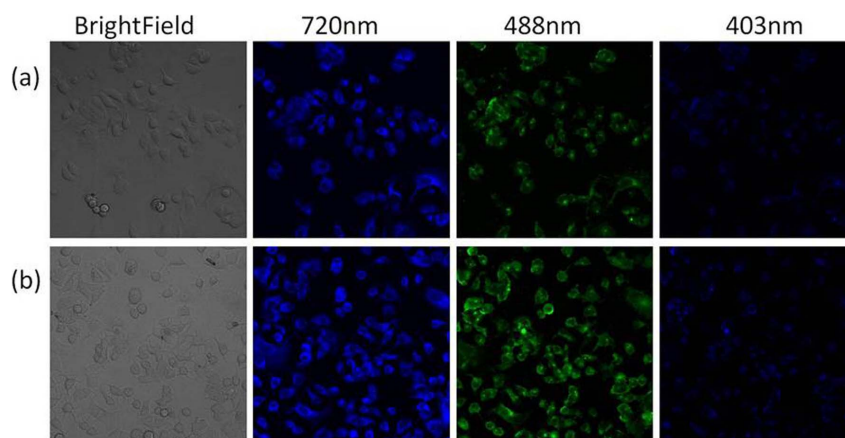

Figure 6 | CLSM images of Mn$_3$[Co(CN)$_6$]$_2$ (a) and Mn$_3$[Co(CN)$_6$]$_2$@SiO$_2$ (b) nanocubes in bright-field, two-photon fluorescence excited by 720 nm femtosecond laser pulses and CLSM excited with 488 nm and 403 nm laser beams, respectively.

Upon biphotonic excitation at 720 nm, both $Mn_3[Co(CN)_6]_2$ and $Mn_3[Co(CN)_6]_2@SiO_2$ nanocubes displayed outstanding fluorescence in the visible spectrum. This TPF imaging technique provides the possibility of long-term imgaing of cellular process with reduced photodamage compared to UV-excited imaging[48]. Recently, it is reported that the photoluminescence of $^4T_1 \rightarrow {}^6A_1$ transition of Mn^{2+} can provide efficient two-photon fluorescent in doped QDs, such as Mn-doped ZnS QDs[42], which demonstrates the possibility of Mn^{2+} ions used in TPF imaging. Compared with Au nanodots with the same fluorescent intensity[50], the concentrations of uncoated and silica-coated $Mn_3[Co(CN)_6]_2$ nanocubes are much lower than that of the reported human insulin-Au nanodots for cellular imaging. Thus, all the results above demonstrate that both uncoated and silica-coated $Mn_3[Co(CN)_6]_2$ nanocubes can be efficiently used as TFP imaging probes. The use of near-infrared-emitting probes could enhance both the tissue depth penetration and imaging sensitivity.

The integration of conventional MRI and TPF probes into a single material such as MOF structured compounds provide a new way to design and synthesis CAs. The advantages of the as-prepared nanoparticles is that they have low toxicity and long circulation time, suggesting their suitability for clinical applications. Most fluorescent probes might be harmful. For instance, Cd-based QDs are used as excellent fluorescent probes, however these nanocrystals have two intrinsic limitations: photooxidation of QDs can cause the release of cadmium and photoexcited QDs can produce reactive oxygen species (ROS). As a result, a doubt has been shed on the future applicability of Cd-containing QDs, particularly in view of environment regulations[51]. While, in $Mn_3[Co(CN)_6]_2$ nanocubes, Mn, Co and CN^- were composed by strong chemical bonds, which can effectively get rid of the toxicity, resulting in better biocompatibility than some reported CAs[52]. Furthermore, after coated with SiO_2, the toxicity decreases remarkably. Since all the CAs investigated nowadays might aggregate in body to cause some long term toxicity, a single material with low cytotoxicity would be more friendly in bio-applications.

In conclusion, we have prepared efficient CAs, $Mn_3[Co(CN)_6]_2$ nanocubes, which show dual contrast enhancement of both T_1- and T_2-weighted MRI and TPLSM fluorescence imaging. This is the first report that an individual material can act as multimodal contrast agents, overcoming major limitations of current multimodal imaging probes prepared by incorporating QDs and magnetic nanoparticles or paramagnetic Gd ions. Surface modification with silica to form $Mn_3[Co(CN)_6]_2@SiO_2$ core-shell nanocubes was achieved, much better biocompatibility was observed in the core-shell nanocubes by cellular cytotoxicity test, making them suitable for biomedical applications.

Methods

In vitro MR imaging. Magnetic Resonance Images (MRI) were acquired by magnetic resonance scanner (GE Signa HDxt 3.0 Tesla MRI system). T_1-weighted MR images were taken by using a saturation recovery using spin-echo sequence (TE = 10 ms, TR = 4000, 2000, 1000, 500, 200, 100 ms,respectively). T_2*-weighted images were also obtained by Carr-Purcell-Meiboom-Gill method with the RARE sequence using the parameter of TR = 120, TE = 2.328, 6.112, 9.896, 13.68, 17.46, 21.24 ms, the filp angle = 30°, bandwidth = 31.25 Hz, FOV 180 × 180 mm², slice thickness = 3 mm without gap.

In vivo MR imaging. Sprague-Dawley (SD) mice weighting 250–280 g were imaged on a 3 T MRI system (GE Signa HDX 3.0 T). High-resolution $Mn_3[Co(CN)_6]_2@SiO_2$ nanocube contrast enhanced multi-slice MR images were obtained from each mouse brain using a fast spin-echo T_1-weighted MRI sequence (repetition time (TR)/echo time (TE) = 780/19.6 ms, number of exitations (NEX) = 2, echo train length = 2, 0.188 × 0.188 mm² in plane resolution with a slice thickness of 2 mm and 10 slices), and a fast spin-echo T_2-weighted MRI sequence (repetition time (TR)/echo time (TE) = 3000/110 ms, number of exitations (NEX) = 2, echo train length = 2, 0.188 × 0.188 mm² in plane resolution with a slice thickness of 2 mm and 10 slices).

All the animal experiment were permitted by the Ethical Committee of the experimental animal center of Medical University of Anhui, China. All the animal experiments and feeding were carried out in accordance with the guidelines of the Ethical Committee of the experimental animal center of Medical University of Anhui, China.

CLSM and TPF measurement. HeLa cells were seeded onto sterile, acid-treated 12-mm coverslips in 24-well plates (Corning Glass Works, Corning, NY, USA). Images were taken with a laser scanning microscope (Zeiss L SM 710) using a 63_1.3 numerical aperture PlanApo objective.

1. Helm, L. Relaxivity in paramagnetic systems: Theory and mechanisms. *Prog Nucl Mag Res Sp* **49**, 45–64 (2006).
2. Gilad, A. A. *et al.* Artificial reporter gene providing MRI contrast based on proton exchange. *Nat Biotechnol* **25**, 217–219 (2007).
3. Major, J. L. & Meade, T. J. Bioresponsive, Cell-Penetrating, and Multimeric MR Contrast Agents. *Accounts Chem Res* **42**, 893–903 (2009).
4. Weissleder, R. A clearer vision for in vivo imaging. *Nat Biotechnol* **19**, 316–317 (2001).
5. Louie, A. Y. Multimodality Imaging Probes: Design and Challenges. *Chem Rev* **110**, 3146–3195 (2010).
6. Nyk, M., Kumar, R., Ohulchanskyy, T. Y., Bergey, E. J. & Prasad, P. N. High Contrast in Vitro and in Vivo Photoluminescence Bioimaging Using Near Infrared to Near Infrared Up-Conversion in TM^{3+} and Yb^{3+} Doped Fluoride Nanophosphors. *Nano Lett* **8**, 3834–3838 (2008).
7. Ow, H. *et al.* Bright and stable core-shell fluorescent silica nanoparticles. *Nano Lett* **5**, 113–117 (2005).
8. Caravan, P., Ellison, J. J., McMurry, T. J. & Lauffer, R. B. Gadolinium(III) chelates as MRI contrast agents: Structure, dynamics, and applications. *Chem Rev* **99**, 2293–2352 (1999).
9. Na, H. B. & Hyeon, T. Nanostructured T1 MRI contrast agents. *J Mater Chem* **19**, 6267–6273 (2009).
10. Na, H. B., Song, I. C. & Hyeon, T. Inorganic Nanoparticles for MRI Contrast Agents. *Adv Mater* **21**, 2133–2148 (2009).
11. Caravan, P. Strategies for increasing the sensitivity of gadolinium based MRI contrast agents. *Chem Soc Rev* **35**, 512–523 (2006).
12. Weinmann, H. J., Ebert, W., Misselwitz, B. & Schmitt-Willich, H. Tissue-specific MR contrast agents. *Eur J Radiol* **46**, 33–44 (2003).
13. Frullano, L. & Meade, T. J. Multimodal MRI contrast agents. *J Biol Inorg Chem* **12**, 939–949 (2007).
14. Stratta, P., Canavese, C. & Aime, S. Gadolinium-enhanced magnetic resonance imaging, renal failure and nephrogenic systemic fibrosis/nephrogenic fibrosing dermopathy. *Curr Med Chem* **15**, 1229–1235 (2008).
15. Lee, Y. C. *et al.* The Use of Silica Coated MnO Nanoparticles to Control MRI Relaxivity in Response to Specific Physiological Changes. *Biomaterials* **33**, 3560–3567 (2012).
16. An, K. *et al.* Synthesis of Uniform Hollow Oxide Nanoparticles through Nanoscale Acid Etching. *Nano Lett* **8**, 4252–4258 (2008).
17. Dias, M. H. M. & Lauterbur, P. C. Ferromagnetic Particles as Contrast Agents for Magnetic-Resonance-Imaging of Liver and Spleen. *Magn Reson Med* **3**, 328–330 (1986).
18. Semelka, R. C. & Helmberger, T. K. G. Contrast agents for MR imaging of the liver. *Radiology* **218**, 27–38 (2001).
19. Schnorr, J. *et al.* Focal liver lesions: SPIO-, gadolinium-, and ferucarbotran-enhanced dynamic T1-weighted and delayed T2-weighted MR imaging in rabbits. *Radiology* **240**, 90–100 (2006).
20. Seo, W. S. *et al.* FeCo/graphitic-shell nanocrystals as advanced magnetic-resonance-imaging and near-infrared agents. *Nat Mater* **5**, 971–976 (2006).
21. Yang, H. *et al.* Targeted dual-contrast T1- and T2-weighted magnetic resonance imaging of tumors using multifunctional gadolinium-labeled superparamagnetic iron oxide nanoparticles. *Biomaterials* **32**, 4584–4593 (2011).
22. Im, G. H. *et al.* Fe_3O_4/MnO hybrid nanocrystals as a dual contrast agent for both T1- and T2-weighted liver MRI. *Biomaterials* **34**, 2069–2076 (2013).
23. Choi, J. S. *et al.* Self-Confirming "AND" Logic Nanoparticles for Fault-Free MRI. *J Am Chem Soc* **132**, 11015–11017 (2010).
24. Aparicio-Ixta, L. *et al.* Two-photon excited fluorescence of silica nanoparticles loaded with a fluorene-based monomer and its cross-conjugated polymer: their application to cell imaging. *Nanoscale* **4**, 7751–7759 (2012).
25. Gao, X. H., Cui, Y. Y., Levenson, R. M., Chung, L. W. K. & Nie, S. M. In vivo cancer targeting and imaging with semiconductor quantum dots. *Nat Biotechnol* **22**, 969–976 (2004).
26. Huang, X. H., Neretina, S. & El-Sayed, M. A. Gold Nanorods: From Synthesis and Properties to Biological and Biomedical Applications. *Adv Mater* **21**, 4880–4910 (2009).
27. Terenziani, F., Katan, C., Badaeva, E., Tretiak, S. & Blanchard-Desce, M. Enhanced Two-Photon Absorption of Organic Chromophores: Theoretical and Experimental Assessments. *Adv Mater* **20**, 4641–4678 (2008).
28. Veiseh, O. *et al.* Optical and MRI Multifunctional Nanoprobe for Targeting Gliomas. *Nano Lett* **5**, 1003–1008 (2005).
29. Jennings, L. E. & Long, N. J. 'Two is better than one'-probes for dual-modality molecular imaging. *Chem Commun*, 3511–3524 (2009).
30. Kim, T. *et al.* Mesoporous Silica-Coated Hollow Manganese Oxide Nanoparticles as Positive T-1 Contrast Agents for Labeling and MRI Tracking of Adipose-Derived Mesenchyrnal Stem Cells. *J Am Chem Soc* **133**, 2955–2961 (2011).

31. Huxford, R. C., deKrafft, K. E., Boyle, W. S., Liu, D. M. & Lin, W. B. Lipid-coated nanoscale coordination polymers for targeted delivery of antifolates to cancer cells. *Chem Sci* **3**, 198–204 (2012).

32. Liong, M. *et al.* Multifunctional inorganic nanoparticles for imaging, targeting, and drug delivery. *Acs Nano* **2**, 889–896 (2008).

33. Dong, W. J. *et al.* Facile Synthesis of Monodisperse Superparamagnetic Fe_3O_4 Core@hybrid@Au Shell Nanocomposite for Bimodal Imaging and Photothermal Therapy. *Adv Mater* **23**, 5392–5397 (2011).

34. Schladt, T. D. *et al.* Au@MnO Nanoflowers: Hybrid Nanocomposites for Selective Dual Functionalization and Imaging. *Angew Chem Int Edit* **49**, 3976–3980 (2010).

35. Bruns, O. T. *et al.* Real-time magnetic resonance imaging and quantification of lipoprotein metabolism in vivo using nanocrystals. *Nat Nanotechnol* **4**, 193–201 (2009).

36. Chen, J. *et al.* Multifunctional Fe_3O_4@C@Ag hybrid nanoparticles as dual modal imaging probes and near-infrared light-responsive drug delivery platform. *Biomaterials* **34**, 571–581 (2013).

37. Xu, Z., Hou, Y. & Sun, S. Magnetic Core/Shell Fe_3O_4/Au and Fe_3O_4/Au/Ag Nanoparticles with Tunable Plasmonic Properties. *J Am Chem Soc* **129**, 8698–8699 (2007).

38. Zipfel, W. R., Williams, R. M. & Webb, W. W. Nonlinear magic: multiphoton microscopy in the biosciences. *Nat Biotechnol* **21**, 1368–1376 (2003).

39. Shokouhimehr, M. *et al.* Dual purpose Prussian blue nanoparticles for cellular imaging and drug delivery: a new generation of T-1-weighted MRI contrast and small molecule delivery agents. *J Mater Chem* **20**, 5251–5259 (2010).

40. Shin, J. M. *et al.* Hollow Manganese Oxide Nanoparticles as Multifunctional Agents for Magnetic Resonance Imaging and Drug Delivery. *Angew Chem Int Edit* **48**, 321–324 (2009).

41. Tanaka, M., Qi, J. & Masumoto, Y. Comparison of energy levels of Mn^{2+} in nanosized- and bulk-ZnS crystals. *J Lumin* **87–89**, 472–474 (2000).

42. Geszke-Moritz, M. *et al.* Thioglycerol-capped Mn-doped ZnS quantum dot bioconjugates as efficient two-photon fluorescent nano-probes for bioimaging. *Journal of Materials Chemistry B* **1**, 698–706 (2013).

43. Hu, L., Zhang, P., Chen, Q. W., Yan, N. & Mei, J. Y. Prussian Blue Analogue Mn-3[Co(CN)(6)](2)center dot nH(2)O porous nanocubes: large-scale synthesis and their CO2 storage properties. *Dalton T* **40**, 5557–5562 (2011).

44. Liang, G. *et al.* Controlled Self-Assembling of Gadolinium Nanoparticles as Smart Molecular Magnetic Resonance Imaging Contrast Agents. *Angewandte Chemie International Edition* **50**, 6283–6286 (2011).

45. Shin, J. M. *et al.* Hollow Manganese Oxide Nanoparticles as Multifunctional Agents for Magnetic Resonance Imaging and Drug Delivery. *Angew Chem Int Edit* **48**, 321–324 (2009).

46. Salazar-Alvarez, G., Sort, J., Surinach, S., Baro, M. D. & Nogues, J. Synthesis and size-dependent exchange bias in inverted core-shell MnO vertical bar Mn_3O_4 nanoparticles. *J Am Chem Soc* **129**, 9102–9108 (2007).

47. Duncan, A. K., Klemm, P. J., Raymond, K. N. & Landry, C. C. Silica Microparticles as a Solid Support for Gadolinium Phosphonate Magnetic Resonance Imaging Contrast Agents. *J Am Chem Soc* **134**, 8046–8049 (2012).

48. Chen, F. *et al.* Gd^{3+}-Ion-Doped Upconversion Nanoprobes: Relaxivity Mechanism Probing and Sensitivity Optimization. *Adv Funct Mater* **23**, 298–307 (2013).

49. Wang, S. & Westmoreland, T. D. Correlation of Relaxivity with Coordination Number in Six-, Seven-, and Eight-Coordinate Mn(II) Complexes of Pendant-Arm Cyclen Derivatives. *Inorg Chem* **48**, 719–727 (2009).

50. Liu, C.-L. *et al.* In vivo Metabolic Imaging of Insulin with Multiphoton Fluorescence of Human Insulin–Au Nanodots. *Small* (2012), DOI: 10.1002/smll.201201887.

51. Schneider, R. *et al.* The exposure of bacteria to CdTe-core quantum dots: the importance of surface chemistry on cytotoxicity. *Nanotechnology* **20**, 225101–225111 (2009).

52. Cai, H. D. *et al.* Facile assembly of Fe_3O_4@Au nanocomposite particles for dual mode magnetic resonance and computed tomography imaging applications. *J Mater Chem* **22**, 15110–15120 (2012).

Acknowledgements

Author contributions

Q.W.C. raised the research proposal, analysed data. Y.M.H. and L.H. designed all experiments. Y.M.H. and Q.W.C. wrote the manuscript. Y.M.H. and T.T.Z. performed and analyzed all experiments. Y.M.H., T.T.Z. and H.B.W. performed in vivo experiments. J.J.Z. was responsible for cell culture work. Z.G. and Z.B.L. performed all CLSM imaging experiments and other cell culture related work. H.Z. drew schematic diagrams.

Additional information

Supplementary information accompanies this paper at http://www.nature.com/scientificreports

Competing financial interests: The authors declare no competing financial interests.

How to cite this article: Huang, Y. *et al.* $Mn_3[Co(CN)_6]_2$@SiO_2 Core-shell Nanocubes: Novel bimodal contrast agents for MRI and optical imaging. *Sci. Rep.* **3**, 2647; DOI:10.1038/srep02647 (2013).